

## Constrained Gaussian-process bridge prior for neutron-star equation-of-state inference

TYLER GORDA <sup>1,2</sup>, OLEG KOMOLTSEV <sup>3</sup>, ALEKSI KURKELA <sup>4</sup> AND EIRIK SUNDE<sup>4</sup>

<sup>1</sup>*Center for Cosmology and AstroParticle Physics (CCAPP), Ohio State University, Columbus, OH 43210*

<sup>2</sup>*Department of Physics, The Ohio State University, Columbus, OH 43210, USA*

<sup>3</sup>*Institut für Theoretische Physik, Goethe Universität, Max-von-Laue-Str. 1, 60438 Frankfurt am Main, Germany*

<sup>4</sup>*Faculty of Science and Technology, University of Stavanger, 4036 Stavanger, Norway*

(Dated: May 12, 2026)

### ABSTRACT

We set forth a new method for generating model-agnostic, nonparametric priors for neutron star equation-of-state inference that are stable, causal and thermodynamically consistent by construction. This generalizes Gaussian processes to include global thermodynamic constraints, specifically allowing the inclusion of any number of training points in the form  $(\mu, n, p)$  while retaining thermodynamic consistency between them. The method is based on constructing constrained Gaussian-process bridges, whose correlation properties can be tuned at will allowing flexibility between a conservative prior and a theory-informed prior. The method does not require any shooting to obey multiple constraints and provides an efficient and informed way to include both chiral effective field theory and perturbative quantum chromodynamics constraints within the same framework.

### 1. INTRODUCTION

Progress in astrophysical observations of neutron stars (NSs) has opened a pathway into studying the densest matter known to exist, found deep within their cores (P. Demorest et al. 2010; J. Antoniadis et al. 2013; B. P. Abbott et al. 2017; T. E. Riley et al. 2019; M. C. Miller et al. 2019). These cores can reach densities up to seven times the nuclear saturation density,  $n_s \approx 0.16 \text{ fm}^{-3}$ , corresponding to values exceeding twice the density inside of a neutron. Understanding the phase structure and properties of baryonic matter under such extreme conditions is of great interest (E. Annala et al. 2020).

Inferring the microphysical conditions within neutron-star cores from macroscopic observables relies on equation-of-state (EoS) inference, which connects the thermodynamic properties of dense matter to the global properties of neutron stars. Each candidate EoS predicts characteristic relations among stellar masses, radii, and tidal deformabilities, as well as the gravitational-wave spectra produced during binary mergers (J. R. Oppenheimer & G. M. Volkoff 1939; R. C. Tolman 1939; T. Hinderer et al. 2010; L. Baiotti & L. Rezzolla 2017; C. Ecker et al. 2025). Comparing these theoretical predictions with astrophysical observations enables one to rule out microphysical models that are inconsistent with current neutron-star data.

Two main strategies have been pursued to exploit the growing body of neutron-star observations. In the first

approach, the EoS is derived from microphysical models of dense matter, constructed under specific theoretical assumptions and approximations. These models, or their parameter ranges, can then be constrained or excluded by observational data (M. Oertel et al. 2017; G. Baym et al. 2018; J. Cartaxo et al. 2025).

With the increasing abundance and precision of neutron star observations, a complementary model-agnostic strategy for EoS inference has become widely adopted (K. Hebeler et al. 2013; A. Kurkela et al. 2014; A. W. Steiner et al. 2016; E. Annala et al. 2018; I. Tews et al. 2018; B. P. Abbott et al. 2019; P. Landry & R. Essick 2019; E. Annala et al. 2020; C. D. Capano et al. 2020; P. Landry et al. 2020; R. Essick et al. 2020; T. Dietrich et al. 2020; M. Al-Mamun et al. 2021; G. Raaijmakers et al. 2021; M. C. Miller et al. 2021; S. Huth et al. 2022; Y. Lim & J. W. Holt 2022; Y. Fujimoto et al. 2024; H. Koehn et al. 2025). In this framework, a large ensemble of trial EoSs is generated using flexible mathematical representations—such as piecewise polytropes, piecewise speed-of-sound parameterizations, spectral expansions, or Gaussian processes—and subsequently compared against observational data. Those inconsistent with the measurements are ruled out, typically through a Bayesian statistical framework, leaving a model-agnostic estimate of the allowed EoS parameter space. Although this approach does not assume any specific microscopic model, the inferred features of the EoS

can nonetheless provide valuable insights into the underlying microphysics (E. Annala et al. 2020, 2023), including possible phase transitions in neutron-star cores (T. Gorda et al. 2023a; D. Mroczek et al. 2024; O. Komoltsev 2024; R. Essick et al. 2023).

Although model-agnostic inference does not assume a specific microscopic model, it is not fully model-independent and the choice of prior strongly influences the posterior, especially at densities where data is scarce. Priors encode essential physical assumptions—namely that the EoS must remain thermodynamically consistent, mechanically stable, and causal, with the speed of sound below the speed of light at all densities. They can also incorporate theoretical input where first-principles calculations provide controlled constraints. Two main strategies are commonly employed. In the first, the prior is anchored to nuclear-theory calculations at densities up to nuclear saturation and extrapolated to higher densities (K. Hebeler et al. 2013). In the second, high-density constraints from perturbative quantum chromodynamics (pQCD) are additionally imposed, and the EoS is interpolated between the nuclear and pQCD regimes around  $20\text{--}40 n_s$  to obtain a family of models that is consistent at all densities (A. Kurkela et al. 2014).

The extent to which pQCD inputs influence EoS inference at neutron-star densities has been widely discussed, and their qualitative effect of softening the EoS at the highest densities is well established (T. Gorda et al. 2023b; R. Somasundaram et al. 2023; O. Komoltsev et al. 2024; S. Altiparmak et al. 2022; H. Koehn et al. 2025; E. Finch et al. 2025; O. Komoltsev 2025). Implementing priors that simultaneously enforce thermodynamic consistency, causality, and stability while incorporating pQCD constraints poses significant technical challenges, as these requirements strongly restrict the functional space of admissible EoSs. Such constraints can be satisfied within parametric priors—such as piecewise polytropes (A. Kurkela et al. 2014) or piecewise speed-of-sound interpolations (E. Annala et al. 2020)—however, it has been shown that parametric representations may act as biased estimators of the EoS leading to uncontrolled correlations among inferred quantities (I. Legred et al. 2022). Nonparametric Gaussian-process (GP) priors alleviate some of these issues but make it difficult to impose all physical constraints simultaneously.

Different strategies have been proposed to address these challenges. In T. Gorda et al. (2023b), the GP prior was extended up to an intermediate demarcation density above the range realized in stable neutron stars, while the pQCD input at higher densities was incorporated through a maximally conservative criterion that excludes any EoS inconsistent with a mechanically sta-

ble, causal and thermodynamically consistent connection to the pQCD EoS (O. Komoltsev & A. Kurkela 2022). This treatment effectively separates the EoS behavior below and above the demarcation density, introducing dependence on this matching point and allowing very stiff or soft behavior at higher densities, without explicitly inferring the EoS beyond the demarcation region. In an alternative approach (E. Finch et al. 2025), the GP prior is simply extended to pQCD densities, removing the need for an intermediate likelihood function; however, because the pQCD constraints are not imposed directly on the prior, most generated EoSs receive very small posterior weights and are rejected. In another alternative approach using Bayesian Model mixing (A. C. Semposki et al. 2025), chiral-effective-field-theory (EFT) and pQCD information is used within their respective regime of validity to condition a GP of the pressure divided by the noninteracting pressure as a function of density. This technique allows one to incorporate both the low- and high-density information at the same time, but it does not by construction impose causality at intermediate densities.

In this work, we propose a new method to generate the prior by constructing a constrained GP-bridge-type process between low- and high-density constraints, addressing the current shortcomings of non-parametric interpolation.

An ordinary GP bridge (D. Gasbarra et al. 2007) with a Gaussian covariance structure—corresponding to a radial basis function (RBF) kernel—can be constructed in two steps. In the first step, the speed of sound between the two end points is drawn from uncorrelated white noise. In the second step, the RBF covariance structure is imposed through deterministic smoothing governed by an appropriate diffusion equation, producing continuous interpolation functions whose correlation lengths are determined by the diffusion parameters. Since the diffusion induces only pairwise correlations, this linear smoothing procedure results in a GP with an RBF kernel.

However, such an approach does not naturally satisfy the thermodynamic consistency conditions of the EoS. To incorporate these constraints, we propose an alternative procedure. Instead of starting from white noise, we generate a space of maximally noisy EoSs through a self-similar (fractal) refinement of the EoS, producing structure across all density scales within the allowed functional space formulated in O. Komoltsev & A. Kurkela (2022). This construction yields EoSs with minimal short-range correlations, but with the non-Gaussian long-range correlations required to satisfy global physical constraints. The desired short-range

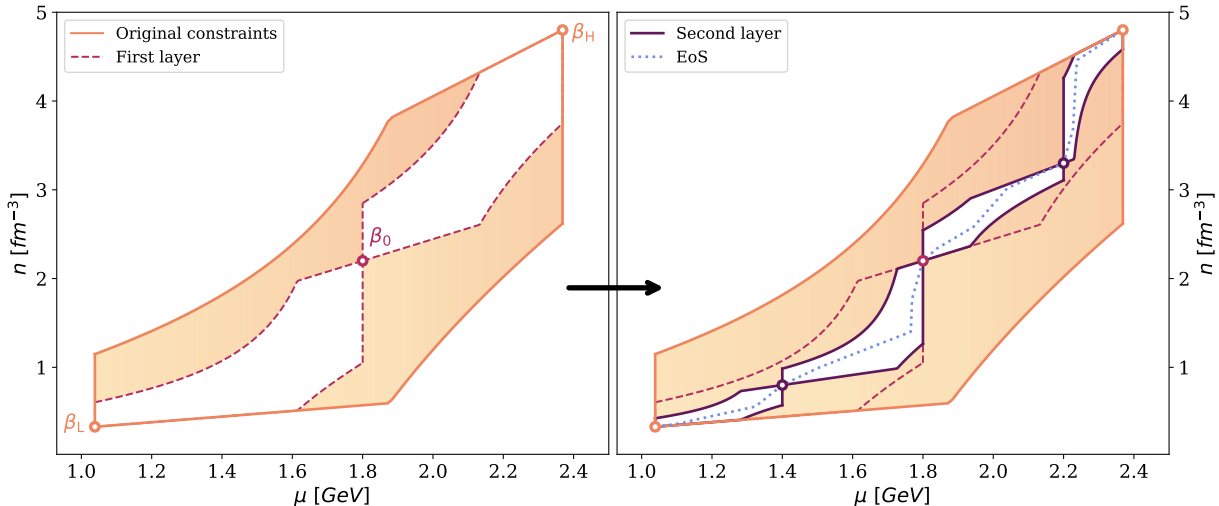


**Figure 1.** Example of a two-step self-similar refinement (fractal). Knowledge of the EoS at low and high densities ( $\beta_L = (\mu_L, n_L, p_L)$  and  $\beta_H = (\mu_H, n_H, p_H)$ ) implies constraints on points  $\beta_0$  lying between them. Once a point  $\beta_0$  is chosen, similar constraints are imposed on the intervals  $[\beta_L, \beta_0]$  and  $[\beta_0, \beta_H]$ . Iteratively refining each interval by introducing new points eventually leads to a complete EoS illustrated by the blue dotted line obtained after multiple iterations passing through the specified points.

RBF covariance structure can then be introduced by applying a diffusion equation, leading to a modified GP-bridge-type construction that preserves the essential thermodynamic properties of the EoS while allowing the correlation length to be tuned as needed.

## 2. METHOD

In this work, we restrict our discussion to zero-temperature matter in  $\beta$ -equilibrium. The method consists of two main steps. First, we generate a noisy, self-similar (fractal) EoS by sampling the full function space allowed by physical constraints. In the second step, local correlations are imposed by applying a diffusion equation in the EoS space.

### 2.1. Robust equation-of-state bounds

To construct the prior, we first sample the function space connecting the low- and high-density limits of the EoS. Each limit is characterized by a triplet of thermodynamic quantities: the chemical potential, number density, and pressure,

$$\beta_L := (\mu_L, n_L, p_L), \quad (1)$$

$$\beta_H := (\mu_H, n_H, p_H). \quad (2)$$

The function space consists of all equations of state represented by  $n(\mu)$  that connect these two limits while remaining mechanically stable, causal, and thermodynamically consistent.

Mechanical stability requires  $n(\mu)$  to be a single-valued function. Causality demands that the function

be monotonic with a sufficiently large derivative,

$$\frac{\mu}{n} \frac{dn}{d\mu} \geq 1, \quad (3)$$

which ensures that the speed of sound does not exceed the speed of light<sup>5</sup>. Thermodynamic consistency requires that the pressure difference between the two limits is correctly reproduced,

$$p_H - p_L = \int_{n_L}^{n_H} dn \mu(n).$$

In O. Komoltsev & A. Kurkela (2022), it was shown that, given  $\beta_L$  and  $\beta_H$ , any valid intermediate  $\beta$  must lie within a volume  $V_{\beta_L, \beta_H}$  (see Fig. 2), defined as follows. For each chemical potential  $\mu$ , the number density must satisfy  $n_{\min}(\mu) < n < n_{\max}(\mu)$ . Furthermore, for each  $\mu$  and  $n$ , the pressure is constrained by  $p_{\min}(\mu) < p < p_{\max}(\mu, n)$ , where all relevant equations are given in App. A.

### 2.2. Self-similar refining:

We generate samples of the EoS function space through a process of self-similar refinement. Starting from the interval  $[\beta_L, \beta_H]$ , we introduce a new intermediate point  $\beta_0$  through which the EoS must pass. As long as this point lies within the allowed volume  $\beta_0 \in V_{\beta_L, \beta_H}$ ,

<sup>5</sup> For non-differentiable functions, the constraint generalizes to excluding functions for which  $\mu n(\mu) \leq \mu' n(\mu')$  for any pair of chemical potentials with  $\mu < \mu'$ .

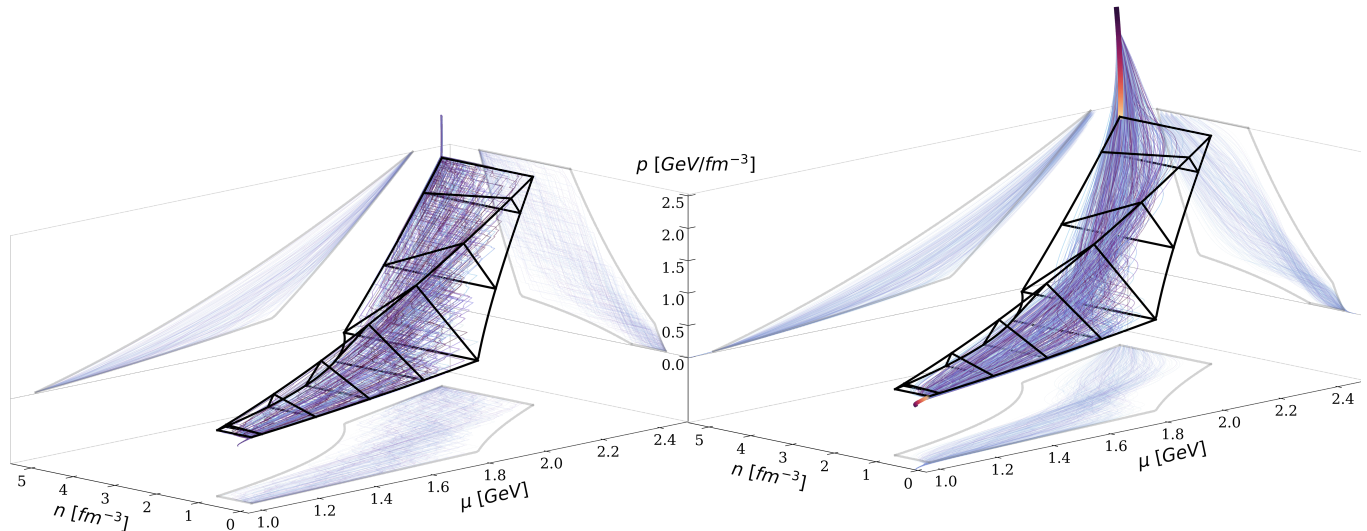


**Figure 2.** Three-dimensional rendering of the volume in the  $(\mu, n, p)$  that can be reached by a stable, causal and consistent EoS interpolating between known low- and high-density limits arising from chiral EFT and perturbative QCD. The limits are depicted as the thick lines emerging from the lower-right and upper-left corners of the volume. (Left) Sample of fractal EoSs constructed using 10 iterations of the self-similar refinement process discussed in Sec. 2.2. The coloring of the EoSs is arbitrary and used solely to improve visual clarity. (Right) Sample of GP-bridge EoSs constructed from the self-similar EoSs by diffusive smoothing as described in Sec. 3.

there exists at least one function that satisfies all physical constraints and passes through it.

The interval  $[\beta_L, \beta_H]$  is then divided into two subintervals,  $[\beta_L, \beta_0]$  and  $[\beta_0, \beta_H]$ . Each subinterval can be further refined by selecting new points from the corresponding subvolumes  $\mathcal{V}_{L0}$  and  $\mathcal{V}_{0H}$ . Iterating this procedure recursively generates EoSs that span the entire space of allowed equations of state while developing structure on all density scales. See Fig. 1 for an illustration of this refinement process.

While the geometry of the function space is dictated by physical constraints, defining a prior over this space requires specifying a probability measure that determines how new points are sampled within the allowed volumes  $\mathcal{V}_{\beta, \beta'}$ . This choice corresponds to specifying the prior distribution. In the present work, we select intermediate points from a uniform distribution  $\mathcal{U}_{\beta, \beta'}$  within each allowed volume, using a Euclidean metric in  $(\mu, n, p)$ -space. Other sampling prescriptions could naturally be adopted, leading to different implicit priors over the EoS space. The details how we perform the uniform sampling are relegated to App. B.

Fig. 2 (left) illustrates a sample of such equations of state constructed using 10 layers in the three-dimensional  $(\mu, n, p)$  - space, together with their projections onto the corresponding two-dimensional planes at fixed values of  $\beta_L$  and  $\beta_H$ . The values of  $\beta_L$  and  $\beta_H$  in this figure are illustrative of the values arising from chiral EFT and pQCD at their domains of applicability.

### 2.3. Introducing local Gaussian correlations

The above discussed method of generating self-similar refinement processes leads to EoSs  $\mu(n)$  that have structures at all scales. For both numerical and physical reasons, we wish to be able to impose a nonzero correlation length to these functions. We do so by applying a heat-kernel smoothing to the resulting processes to produce the desired covariance structure and correlation length.

Specifically, we find it advantageous to diffuse the chemical potential as function of  $n$ ,  $\mu(n)$ . We elevate the equation of state to be a function of an unphysical flow time  $\tau$ ,  $\mu(n, \tau)$ . The evolution in the flow time is then determined by the heat equation

$$\partial_\tau \mu(n, \tau) = \partial_n [D(n) \partial_n \mu(n, \tau)], \quad (4)$$

with the initial condition  $\mu(n, 0) = \mu(n)$  and a density-dependent diffusion coefficient  $D(n)$  and imposing Dirichlet boundary conditions. This procedure increases the correlation between points which are within the diffusion scale  $\delta n \sim \sqrt{4D\tau}$  from each other.

It is crucial that the diffusion process preserves the EoS within the physically allowed function space. The condition of mechanical stability requires  $\mu(n)$  to be a monotonically increasing function. Since the initial configuration is monotonic by construction, diffusion cannot generate non-monotonocities as long as the diffusion coefficient remains strictly positive. Similarly, the condition of causality imposes an upper bound on the derivative of  $\mu(n)$ ; since the initial configuration satisfies this

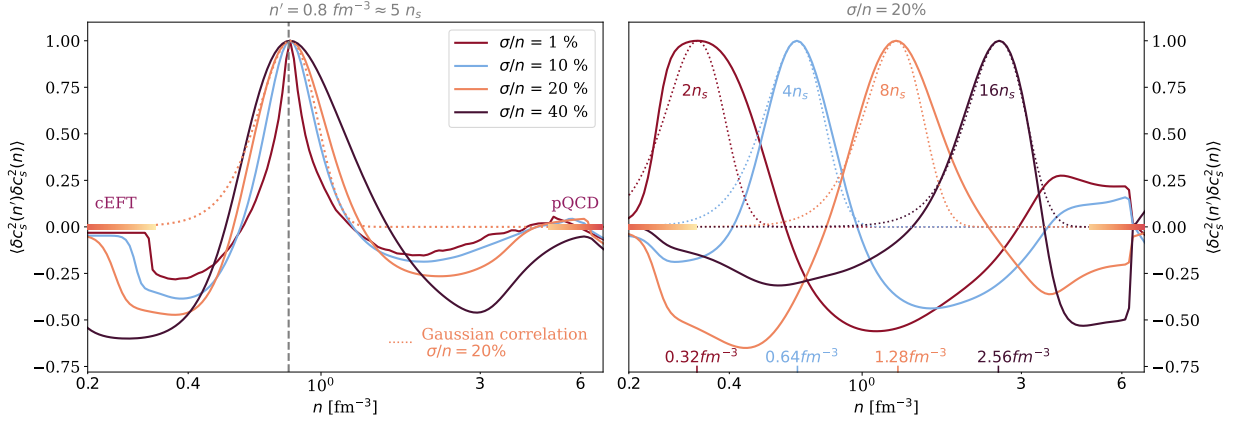


**Figure 3.** The two-point correlation function of the sound speed,  $\langle \delta c_s^2(n') \delta c_s^2(n) \rangle$ , showing correlations between values at  $n' = 0.8 \text{ fm}^{-3}$  and different  $n$  for varying levels of diffusion (left panel), and for a fixed amount of diffusion with varying  $n'$  (right panel). Thin dashed lines show the corresponding Gaussian correlations, with correlation lengths set by the amount of diffusion,  $\sigma = \sqrt{4D(n')t}$ . The local correlations closely follow the Gaussian form, but the global structure imposed by physical constraints produces a long-range anti-correlation.

constraint, the diffusion process cannot produce superluminal speeds of sound in the diffusion domain as long as

$$D'' - \frac{D'}{n} \leq 0, \quad (5)$$

see App. C for details.

Finally, the diffusion equation conserves the energy density,

$$\varepsilon' - \varepsilon = \int_n^{n'} dn \mu(n), \quad (6)$$

and hence preserves thermodynamic consistency within the domain, given that  $\varepsilon = -p + \mu n$ . At the boundaries, however, the energy density may “flow” through the edges of the interval,

$$\partial_\tau(\varepsilon_H - \varepsilon_L) = \partial_\tau \int_{n_L}^{n_H} dn \mu(n, \tau) = [D(n) \partial_n \mu(n, \tau)]_{n_L}^{n_H}, \quad (7)$$

leading to a mild violation of thermodynamic consistency in  $\varepsilon_H$ . This effect can be mitigated by tapering the diffusion coefficient  $D(n)$  to zero near the boundaries or by reinjecting the corresponding energy after the evolution. In practice, we find that this deviation alters the energy density at  $\mu_H$  only at the percent level—well below the current theoretical uncertainty of chiral EFT and pQCD calculations at these densities—and can therefore be safely neglected.

### 2.3.1. Covariance and correlation length of sound speed

In order to connect with the existing literature, we highlight the similarities and differences between our constrained GP bridge construction and the standard GP approaches to modeling the speed of sound (P.

Landry & R. Essick 2019; T. Gorda et al. 2023b). In GP-based frameworks, the process is typically defined through a constant or density-dependent correlation length. Here, we show that by choosing an appropriate functional form for the diffusion coefficient  $D(n)$ , one can control the local correlation length of the sound speed while simultaneously maintaining the non-trivial global correlations implied by the underlying physical constraints.

Locally, for slowly varying  $D(n)$ , the correlation function of the sound-speed fluctuations, defined as  $\delta c_s^2 := c_s^2 - \langle c_s^2 \rangle$ , becomes

$$\begin{aligned} \langle \delta c_s^2(n, \tau) \delta c_s^2(n', \tau) \rangle & \\ &= \int d\xi d\xi' G(n, \xi; \tau) G(n', \xi'; \tau) \langle \delta c_s^2(\xi, 0) \delta c_s^2(\xi', 0) \rangle, \end{aligned} \quad (8)$$

where  $G(n, \xi; \tau)$  is the Green’s function of the diffusion equation. For a nearly white initial correlation in the sound speed,  $\langle \delta c_s^2(\xi, 0) \delta c_s^2(\xi', 0) \rangle \simeq \sigma_s^2 \delta(\xi - \xi')$ , the evolved correlation function is locally approximated by a Gaussian (see App. D for details),

$$\langle \delta c_s^2(n, \tau) \delta c_s^2(n', \tau) \rangle \propto \frac{1}{\sqrt{8\pi D(n)\tau}} \exp\left[-\frac{(n - n')^2}{8D(n)\tau}\right], \quad (9)$$

with a characteristic correlation length  $\sigma = \sqrt{4D(n)\tau}$ . This provides a direct way to control the local correlation length of  $c_s^2$  through the density dependence of  $D(n)$ , offering a flexibility analogous to that of GP kernels, while simultaneously preserving the global physical constraints imposed by the diffusion dynamics.

In the following, we aim to reproduce a correlation length that remains logarithmically constant as a function of density in order to both allow for fine structure

for the EoS at low densities and span the large density range up to pQCD densities; that is, the correlation length from diffusion at all densities corresponds to a fixed fraction of the density,  $\sigma/n = c$ , with  $c$  constant. According to Eq. (9), such a correlation length is obtained by choosing  $D(n)\tau = n^2 c^2/4$ . In practice, we evolve the diffusion equation from  $\tau = 0$  to 1, with a density dependent diffusion coefficient  $D(n) = n^2 c^2/4$ .

Fig. 3 shows the two-point correlation function of the sound speed defined in Eq. (8) evaluated with one of the arguments  $n' = 0.8 \text{ fm}^{-3}$  and as a function of the other density  $n$ . In order to numerically extract the sound speed, we must apply at least a minimal level of diffusion to make the EoS differentiable. The line corresponding to  $c = 1\%$  demonstrates that the self-similar refinement process produces a sharply peaked, yet non-white, correlation function that exhibits a long-range anti-correlation. This feature implies that if the EoS is stiff at low densities, it tends to become soft at higher densities. The reference density in the left figure,  $n' \approx 5 n_s$ , is chosen to be representative of the densities expected in a maximum-mass neutron star. This anticorrelation behavior is consistent with the observation that an EoS capable of supporting a two-solar-mass star, which requires stiffening at intermediate densities, must soften at higher densities (T. Gorda et al. 2023b; O. Komoltsev et al. 2024).

At higher levels of diffusion ( $\sigma/n = 10\%, 20\%$ ), the local correlation approaches a Gaussian form, as expected, and is well reproduced by Eq. (9) (shown as a dotted line). As the correlation length increases, the global anticorrelation becomes stronger. For sufficiently large correlation lengths (40%), the global structure dominates and the overall correlation exceeds the local Gaussian component that would arise in the absence of global constraints.

The right panel of Fig. 3 shows the correlation function at several reference densities,  $n = [2, 4, 8, 16] n_s \approx [0.32, 0.64, 1.28, 2.56] \text{ fm}^{-3}$ , for a fixed  $\sigma/n = 20\%$ . For each density, the dotted line denotes the corresponding Gaussian correlation.

### 3. IMPLEMENTATION

Moving to an application of the framework described above, we now specify the low- and high-density inputs and neutron-star observations used in the present work.

#### 3.1. High- and low-density limits

The outer crust is modeled using the standard BPS equation of state (G. Baym et al. 1971). At densities above  $n_{\text{atmos}} := 0.34 n_s \approx 0.055 \text{ fm}^{-3}$ , we switch to a chiral-EFT-based EoS, describing charge-neutral,  $\beta$ -equilibrated nuclear matter that includes chiral NN and

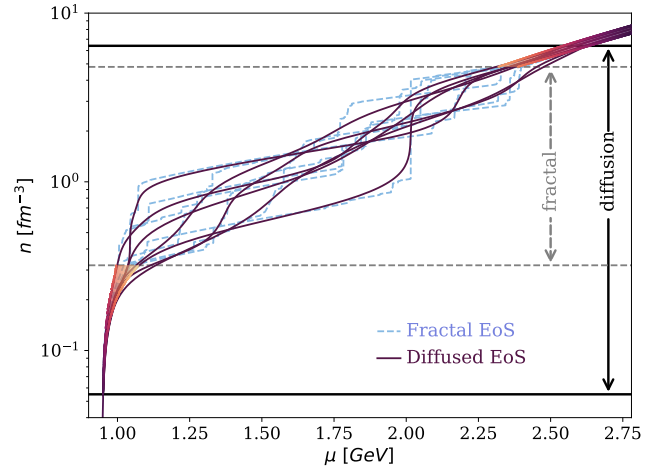


**Figure 4.** The procedure for incorporating the low- and high-density inputs into the construction of the constrained GP bridge. The blue dashed lines correspond to the samples of the fractal EoSs together with their diffused counterparts represented by purple solid lines. The two colored bands correspond to the low- and high-density limits from the chiral EFT and pQCD EoSs. The fractal EoS is constructed from two endpoints,  $\beta_L$  and  $\beta_H$ , obtained from the sampled chiral-EFT and pQCD EoSs at the corresponding densities  $n_L = 2 n_s$  and  $n_H = 30 n_s$ . The diffusion is then performed over the broader density range  $[0.34, 40] n_s$  to ensure a smooth transition of  $c_s^2$  to both limits.

3N interactions up to N3LO order (C. Drischler et al. 2021). In practice, we sample the nuclear EoS within the range considered in C. Drischler et al. (2021) and extend it up to a density of  $n_L := 2 n_s \approx 0.32 \text{ fm}^{-3}$ , thereby generating a set of nuclear EoSs  $\mu_{\text{CEFT}}(n)$  over the interval  $[n_{\text{atmos}}, n_L]$ .

At high densities we take the pQCD EoS from T. Gorda et al. (2021) and extend it down to the density  $n_H := 30 n_s \approx 4.8 \text{ fm}^{-3}$ . The pQCD EoS has an uncertainty quantified by variation of the renormalization scale,  $X$ , which we sample from a log-linear distribution (T. Gorda et al. 2023c) to obtain pQCD EoSs  $\mu_{\text{pQCD}}(n)$ .

The density range between  $[n_L, n_H]$  is then populated with the self-similar fractal EoSs. In the bridge process as described in the previous Section, the primary thermodynamic variables  $\mu$ ,  $n$ , and  $p$  are by construction continuous across the switching points  $n_L$  and  $n_H$ . In order to ensure that also the higher derivatives of  $\mu(n)$ —including the sound speed  $c_s^2$ —vary smoothly, we extend the range where the diffusion is performed beyond the range of the fractal EoSs. Specifically, in the range  $[n_{\text{atmos}}, n_L]$  we perform diffusion but the initial condition is given by the nuclear EoS. Similarly, the initial condition is given by the pQCD EoS between  $n_H$  and  $40 n_s$ .

In Fig. 4, we show several samples of the fractal EoSs in the  $\mu$ - $n$  plane together with their diffused counterparts. The density interval over which the fractal is constructed is indicated by gray dashed lines and corresponds to the range  $[n_L, n_H]$ . The black lines show the limits of the density range,  $[0.34, 40] n_s$ , where diffusion is performed.

### 3.2. Equation-of-state inference

To constrain the prior distribution of the bridge process,  $P(\text{EoS})$ , we condition it on the available neutron-star observations using Bayes' theorem,

$$P(\text{EoS} | \text{Data}) = \frac{P(\text{Data} | \text{EoS}) P(\text{EoS})}{P(\text{Data})}. \quad (10)$$

For the likelihood,  $P(\text{Data} | \text{EoS})$ , we adopt the likelihood function from T. Gorda et al. (2023b) along with some updated measurement data, which incorporates the mass measurements of PSR J0348+0432 (A. Saffer et al. 2025; J. Antoniadis et al. 2013) and PSR J1614–2230 (Z. Arzoumanian et al. 2018; E. Fonseca et al. 2016; P. Demorest et al. 2010), the joint mass–radius constraint on PSR J0740+6620 obtained from NICER observations (E. Fonseca et al. 2021; M. C. Miller et al. 2021; T. E. Riley et al. 2021; A. J. Dittmann et al. 2024), and the tidal-deformability measurement from GW170817 reported by the LIGO/Virgo collaboration (B. P. Abbott et al. 2019). We also incorporate the recent mass measurement (from MeerKAT) and the radius determination (from NICER) for PSR J0614–3329 (L. Mauviard et al. 2025) as well as the radius determination of PSR J0437–4715 from NICER (D. Choudhury et al. 2024). For EoSs with multiple stable branches, we consider only the configurations with largest radius for the same mass, as we are unaware of a production mechanism for the smaller-radius stars.

## 4. RESULTS

In Fig. 5, we compare the EoS of strongly interacting matter from  $0.1 n_s$  to the pQCD regime for four different levels of diffusive correlation,  $\sigma/n = 1\%$ ,  $10\%$ ,  $20\%$ , and  $40\%$ . In the leftmost column, we see that the smallest correlation length covers much of the allowed  $\varepsilon$ - $p$  region from O. Komoltsev & A. Kurkela (2022) at intermediate densities, while progressively increasing the correlation concentrates the prior more towards the center of the allowed region. With increasing correlation length the global structure in  $\varepsilon$ - $p$  and  $c_s^2$ - $n$  becomes more clear.

We also witness a decreased coverage of the full range of  $c_s^2$ , especially for the highest correlation length of  $0.4$ . In all cases, the EoSs in the posterior distribution exhibit a stiffening immediately beyond the chiral-EFT

regime, with shorter correlations showing a larger maximum in  $c_s^2$  with a peak at slightly smaller densities. Beyond this maximum, the posterior EoSs show a softer behavior. In particular, for the two largest correlations considered, the speed of sound exhibits a clear softening onset from  $1 \text{ fm}^{-3} \lesssim n \lesssim 2 \text{ fm}^{-3}$  to roughly the pQCD regime at  $n \approx 4 - 6 \text{ fm}^{-3}$ , consistent with the behavior observed in earlier works (E. Annala et al. 2020; T. Gorda et al. 2023b; S. Altiparmak et al. 2022; E. Annala et al. 2023; O. Komoltsev et al. 2024; E. Finch et al. 2025). The shorter correlation lengths that admit for a stronger sound-speed peak at lower densities tend to favor smaller speeds of sound at high densities (best visible for  $\sigma/n = 20\%$ ) whereas the larger correlation lengths ( $\sigma/n = 40\%$ ) softens the peak, leading to higher speeds of sound at higher densities. We emphasize that this softening takes place over several correlation lengths in these latter two panels, as illustrated by the line segments representing  $\sigma$  in the panels.

We observe that, while the correlation length has a significant effect on the local properties of the EoS, the mass–radius relation—which depends on integrals of the EoS—is largely unaffected by changes in the correlation length. However, we do observe that the prior with the largest correlation length reaches slightly larger radii than any of the others, which we attribute to the fact that EoSs with longer correlation lengths can remain stiff over an extended density range. Finally, the maximum likelihood of a given EoS exhibits an inverse dependence on the correlation length (not shown). This behavior is expected, as EoSs with shorter correlation lengths can rapidly adjust their behavior to remain consistent with a larger fraction of the observational data included in the likelihood, leading to a degree of overfitting.

In Fig. 6 and Fig. 7, we show a posterior sample of 75,000 EoSs drawn from a hierarchical model combining different correlation lengths with a uniform range of  $\sigma/n \in [0.2, 0.4]$ . We again see a stiffer behavior at lower densities, driven by the high-mass pulsar constraint, followed by a softer average behavior at higher densities. In Y. Fujimoto et al. (2022); E. Annala et al. (2023), the trace anomaly  $\Delta := 1/3 - p/\varepsilon$ , the conformal distance  $d_c := \sqrt{\Delta^2 + (d\Delta/d \log \varepsilon)^2}$ , and the pressure normalized to that of a free quark gas at the same baryon chemical potential,  $p/p_{\text{free}}$ , were identified as observables sensitive to the phase structure of matter. The trace anomaly approaches zero in pQCD, which is expected to be a generic feature of nearly conformal quark matter. This behavior is observed at high densities in Fig. 7, while at the central densities reached in the most massive stars negative trace anomalies are favored. Con-

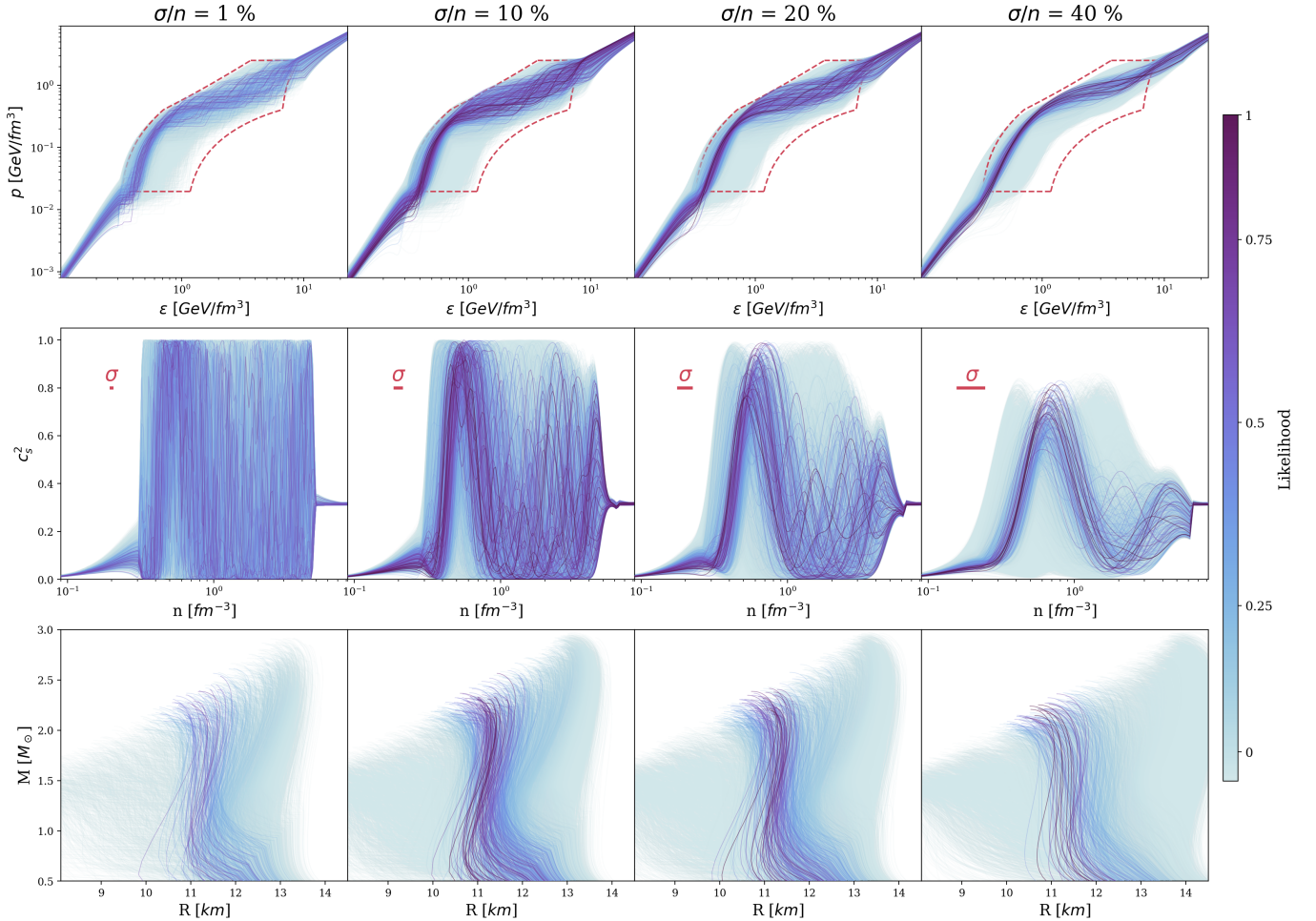


**Figure 5.** Progression of the posterior equation of state ( $\epsilon$  vs  $p$ ), speed of sound ( $c_s^2$  vs  $n$ ) and the mass-radius relation ( $M$  vs  $R$ ) as a function of the relative correlation length  $\sigma/n = 1\%$ ,  $10\%$ ,  $20\%$ , and  $40\%$ . Each EoS drawn from the prior is colored according to the combined likelihood function. The likelihood function is normalized separately to the maximum likelihood for each fixed correlation length. As the correlation length increases, the global structure of the EoS with significant softening at high densities becomes clearer. The bar marked with  $\sigma$  indicates the correlation length associated with each column. The relative correlation length corresponds to a fixed length on a logarithmic axis.

sistent with E. Annala et al. (2023), the variable  $d_c$ , which peaks around densities reached in  $2M_\odot$  stars, decreases at larger densities. At the highest densities reached in stable neutron stars, the central densities in most EoSs satisfy  $d_c < 0.2$ , a value quoted as indicative of quark matter. At still higher densities, the values plateau (with some fluctuations) as pQCD densities are approached. A corresponding behavior is also seen in  $p/p_{\text{free}}$ , which approximately plateaus above chemical potentials of  $\mu \sim 1.25$  GeV. However, given the large uncertainties in the posterior, while the EoS may remain approximately constant—as expected for quark matter—a strong first-order phase transition, manifested as a discontinuity in the  $\mu$ -derivative of  $p/p_{\text{free}}$ , cannot be excluded. This is especially true at densities above those reached in the most massive stars, in agreement with O. Komoltsev (2024).

One advantage of the current technique is that we are able to infer the EoS at all densities with a unified prior. In particular, we can study how the individual observations constrain the high-density part of the EoS beyond the stable neutron-star branch. The individual likelihood functions from selected observations are compared in Fig. 8. We see that all the measurements constrain the EoS even at densities that go well beyond the densities reached in the corresponding stars, due to the global thermodynamic correlations. This is particularly visible for PSR J0614–3329, where EoSs with the lowest pressures above  $\epsilon \gtrsim 2$  GeV/fm<sup>3</sup> receive negligible likelihood. We also find it interesting that all of the measurements besides PSR J0740+6620 resemble each other both qualitatively and quantitatively, favoring smaller radii for the most massive stars, whereas PSR J0740+6620 suggests larger radii. The highest likelihood EoSs from

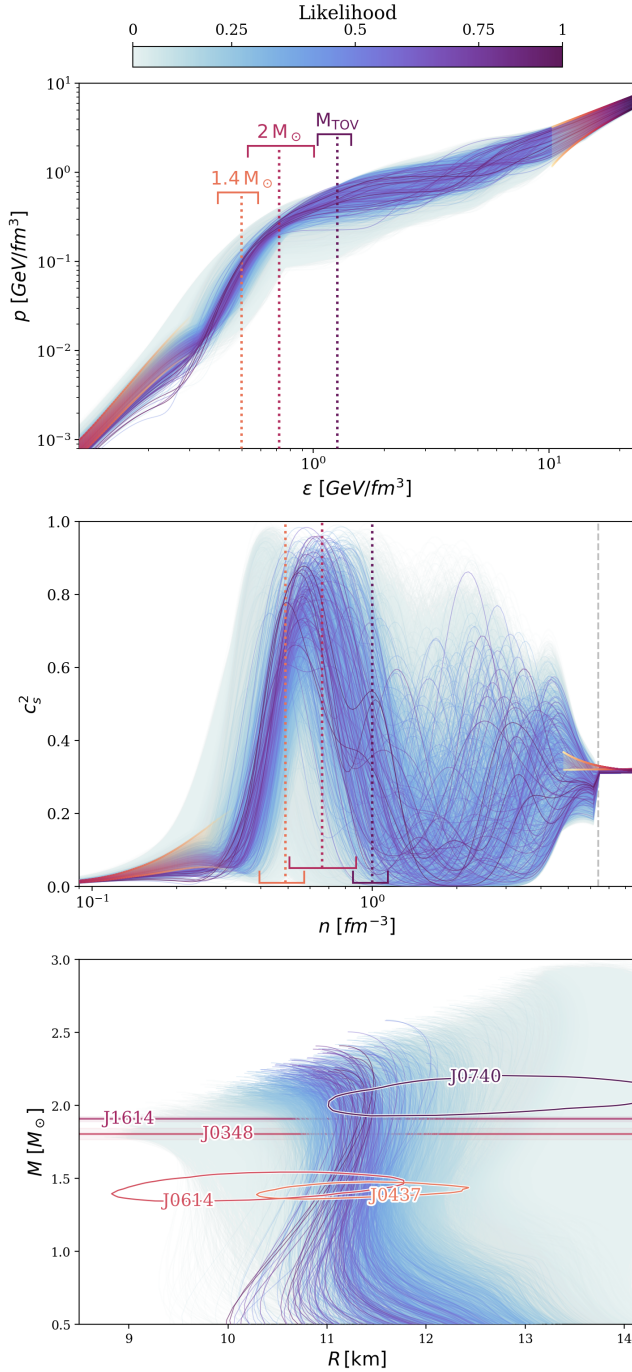


**Figure 6.** Posterior of  $p(\epsilon)$ ,  $c_s^2(n)$  and  $M(R)$  from the hierarchical model discussed in Sec. 4 with the correlation length taken from a uniform distribution  $\sigma/n \in [0.2, 0.4]$ . The dotted vertical lines and the associated bars correspond to the mean and 1- $\sigma$  credible intervals for densities reached in the centers of  $1.4M_\odot$ ,  $2M_\odot$ , and  $M_{\text{TOV}}$  stars, while the contours in the lowest panel represent the 68% credible regions of the corresponding NICER observations.

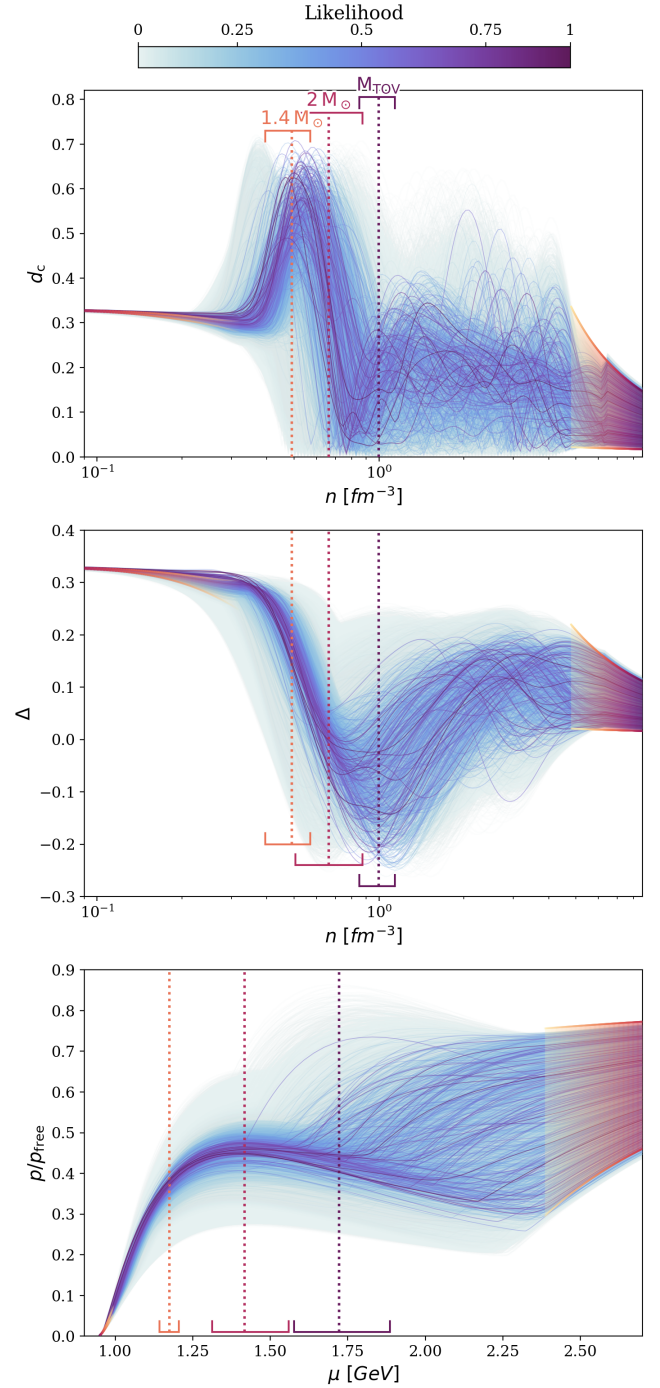


**Figure 7.** Posterior of  $d_c(n)$ ,  $\Delta(n)$ , and  $p/p_{\text{free}}(\mu)$  (see main text for definitions) from the hierarchical model discussed in Sec. 4 with the correlation length taken from a uniform distribution  $\sigma/n \in [0.2, 0.4]$ . The dotted vertical lines and the associated bars correspond to the mean and 1- $\sigma$  credible interval for densities reached in the centers of  $1.4M_\odot$ ,  $2M_\odot$ , and  $M_{\text{TOV}}$  stars.

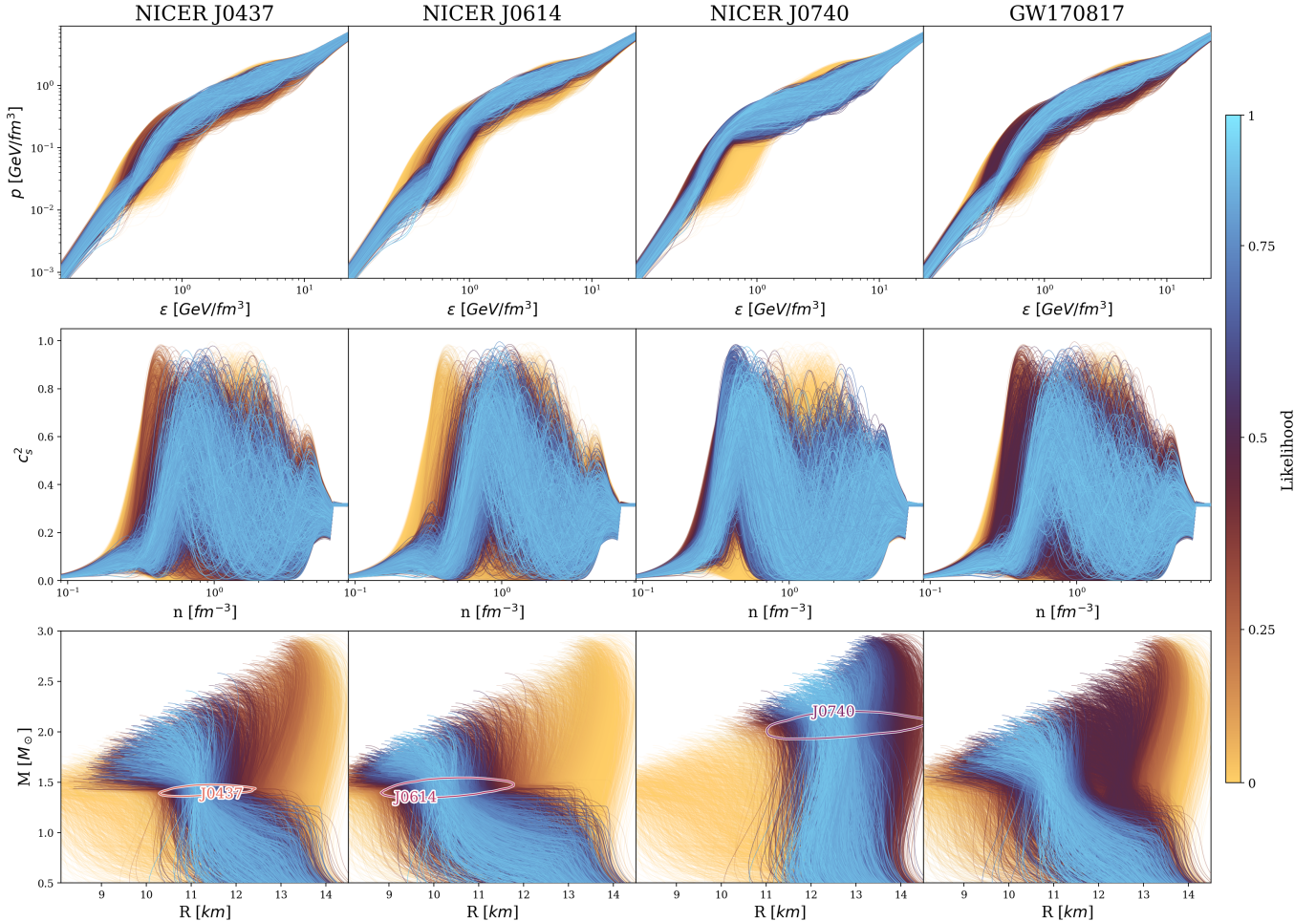


**Figure 8.** A sample of EoSs, colored according to the likelihood functions derived from various individual X-ray and gravitational-wave observations. NICER J0437 corresponds to the simultaneous mass–radius measurement of PSR J0437–4715 from D. Choudhury et al. (2024), NICER J0614 to that of PSR J0614–3329 from L. Mauviard et al. (2025), NICER J0740 to that of PSR J0740+6620 from A. J. Dittmann et al. (2024), and GW170817 to the gravitational-wave observations reported in B. P. Abbott et al. (2019). The prior used here is the hierarchical model discussed in Section 4. The contours in the lowest panel represent the 68% credible regions of the corresponding NICER observations.

all three other measurements are consistent among each other but inconsistent with the highest-likelihood EoSs from PSR J0740+6620. It will be interesting to see whether future, more precise, radius and tidal deformability measurements remain consistent with each other.

## 5. CONCLUSIONS

In this work, we introduced a new nonparametric prior for neutron-star equation-of-state inference based on a constrained Gaussian-process-bridge construction. The method generates equations of state that are thermodynamically consistent, mechanically stable, and causal by construction, while incorporating controlled low- and high-density theoretical inputs from chiral effective field theory and perturbative quantum chromodynamics. Unlike existing nonparametric approaches, it does not rely on shooting procedures, intermediate like-

lihoods, or *ad hoc* switching between EoS representations.

A central feature of the construction is its ability to uniformly explore the full physically allowed EoS volume between the low- and high-density anchors. The resulting prior is maximally flexible within the space of admissible functions, developing structure on all density scales while allowing for controlled local correlations through diffusion. This enables a transparent tuning of the sound-speed correlation length and facilitates direct comparison with standard Gaussian-Process-based priors, while retaining the nontrivial global correlations imposed by physical constraints.

These global constraints induce long-range anticorrelations in the speed of sound: equations of state that stiffen at intermediate densities are generically required to soften at higher densities in order to remain consis-

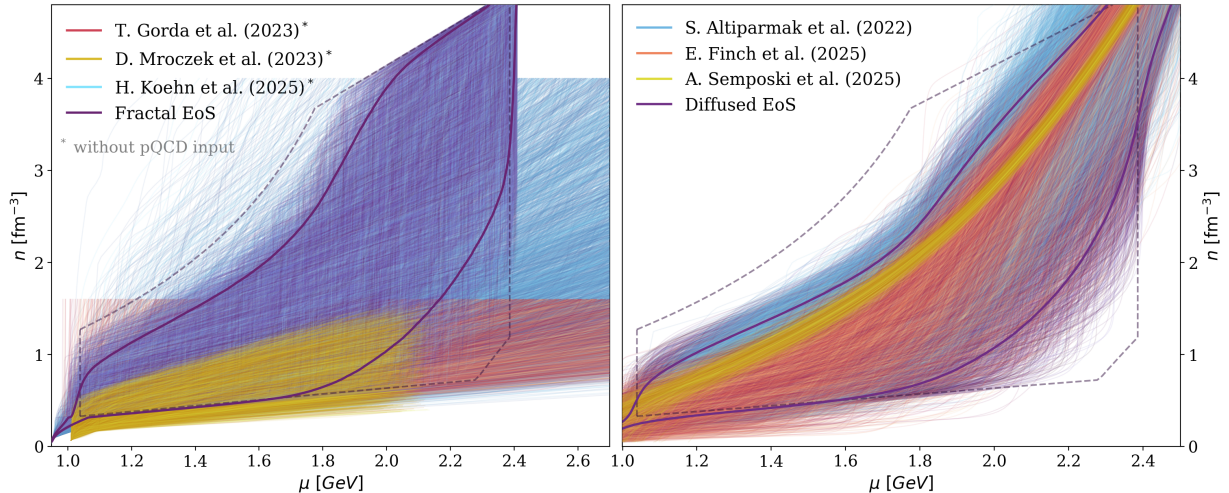


**Figure 9.** A comparison of the sample of priors from previous works with the current method. (Left) The most generic non-diffused fractal EoS prior compared to priors of T. Gorda et al. (2021), D. Mroczek et al. (2024), and H. Koehn et al. (2025). The dashed lines correspond to the boundary of the allowed region when varying the pQCD range of  $X \in [1/2, 2]$  as in T. Gorda et al. (2023b). The thick violet line corresponds to the  $2\text{-}\sigma$  credible interval for the fractal prior. (Right) The diffused GP bridge compared to other priors that include pQCD constraints. The thick lines correspond to the  $2\text{-}\sigma$  credible interval for the diffused prior.

tent with causality, thermodynamic consistency, and the pQCD limit. This behavior emerges naturally from the prior and persists even in the limit of vanishing diffusion, demonstrating that it reflects the global structure of the physically allowed equation-of-state space rather than imposed local correlations. When conditioned on current astrophysical data, the inferred equations of state must remain sufficiently stiff to support two-solar-mass neutron stars, followed by a systematic softening at higher densities that are still realized within stable neutron stars. This qualitative behavior is consistent with previous model-agnostic studies and may be suggestive of phase-transition-like physics in neutron-star cores.

Fig. 9 illustrates several qualitative differences between the constrained GP-bridge prior and existing priors in the literature. The approaches that do not include the high-density pQCD constraints in the prior level explore a significantly larger function space, large parts of which are excluded; this is exemplified by the comparison of the non-diffused fractal EoS with the Gaussian-Process prior of T. Gorda et al. (2023b) (constructed up to  $10 n_s$ ) and the piecewise linear  $c_s^2$  prior of H. Koehn et al. (2025) (constructed up to  $25 n_s$ ) in the left panel. Also shown in the left panel is the modified Gaussian-Process prior of D. Mroczek et al. (2024), which includes points only on the stable neutron-star branch. The model-informed prior, which is constructed around a rapidly stiffening mean, does not fully explore the space of soft EoSs. Compared to the approaches that enforce low- and high-density theoretical constraints, the dif-

ferences are significantly smaller. While the differences between the priors arise to some extent from different choices of correlation lengths and different levels of deliberate modeling bias, a benefit of our scale-invariant fractal construction is that fills the entire allowed volume without extending beyond it, ensuring that no physically admissible behavior is excluded a priori and enabling a broader exploration of high-density EoS trajectories while maintaining a smooth connection to the pQCD anchor. In this sense, the constrained GP-bridge prior should be viewed not merely as a computationally efficient alternative (of the order of seconds for 1000 EoSs), but as a physically motivated framework for encoding prior knowledge about dense matter.

Looking ahead, the constraining power of this framework is expected to improve significantly as pQCD calculations are extended to higher orders. In particular, once pQCD results reach N3LO accuracy with reduced renormalization-scale uncertainties (T. Gorda et al. 2021, 2023d; A. Kärkkäinen et al. 2025), the high-density anchor will become substantially tighter, enabling more precise propagation of first-principles information from quantum chromodynamics to neutron-star densities within the present unified framework.

## AUTHOR CONTRIBUTIONS

Authors are listed in alphabetical order.

## ACKNOWLEDGMENTS

We thank C. Drischler, C. Ecker, H. Koehn, D. Mroczek, and A. Semposki for sharing priors from their respective works. We also thank D. Furnstahl, T. Kleppe,

and L. Rezzolla for interesting discussions. O.K. acknowledges support from the Alexander von Humboldt Foundation through a Humboldt Research Fellowship for Postdoctoral Researchers.

## APPENDIX

## A. EXPRESSIONS FOR THE 3-VOLUME

The volume shown in Fig. 2 (black lines) is defined as follows. For a fixed chemical potential  $\mu$ , the number density is restricted to the interval  $n_{\min}(\mu) \leq n \leq n_{\max}(\mu)$ . For each allowed pair  $(\mu, n)$ , the pressure is further constrained to lie between  $p_{\min}(\mu, n)$  and  $p_{\max}(\mu, n)$ . The analytical expression for  $n_{\min/\max}$  and  $p_{\min/\max}$  are given by:

$$n_{\min}(\mu) = \begin{cases} n_L \mu / \mu_L, & \mu_L \leq \mu \leq \mu_c, \\ \frac{\mu^3 n_H - \mu \mu_H (\mu_H n_H - 2\Delta p)}{(\mu^2 - \mu_L^2) \mu_H}, & \mu_c < \mu \leq \mu_H. \end{cases} \quad (\text{A1})$$

$$n_{\max}(\mu) = \begin{cases} \frac{\mu^3 n_L - \mu_L \mu (\mu_L n_L + 2\Delta p)}{(\mu^2 - \mu_H^2) \mu_L}, & \mu_L \leq \mu < \mu_c, \\ n_H \mu / \mu_H, & \mu_c \leq \mu \leq \mu_H. \end{cases} \quad (\text{A2})$$

$$p_{\min}(\mu) = p_L + \frac{\mu^2 - \mu_L^2}{2\mu} n_{\min}(\mu). \quad (\text{A3})$$

$$p_{\max}(\mu, n) = \begin{cases} p_L + \frac{\mu^2 - \mu_L^2}{2\mu} n, & n \leq n_c(\mu), \\ p_H - \frac{\mu_H^2 - \mu^2}{2\mu} n, & n > n_c(\mu). \end{cases} \quad (\text{A4})$$

With the following auxiliary definitions:

$$\mu_c = \sqrt{\frac{\mu_L \mu_H (\mu_H n_H - \mu_L n_L - 2\Delta p)}{\mu_L n_H - \mu_H n_L}}, \quad (\text{A5})$$

$$\Delta p = p_H - p_L, \quad (\text{A6})$$

$$n_c(\mu) = \frac{n_{\max}(\mu_L)}{\mu_L} \mu = \frac{n_{\min}(\mu_H)}{\mu_H} \mu. \quad (\text{A7})$$

## B. UNIFORM SAMPLING IN THE ALLOWED 3-VOLUME

In order to achieve a uniform sampling on the volume of allowed points of EoS  $V_{\beta_L, \beta_H}$ , which we denote  $\mathcal{U}_{\beta_L, \beta_H}(\beta)$ , using the transformation method, we perform the following steps:

1. Draw  $\mu \in [\mu_L, \mu_H]$ , from the marginalized distribution whose density is given by the area of the triangular slice of  $V_{\beta_L, \beta_H}$  at the value  $\mu$ ; namely,

$$P(\mu) := \int dn dp \mathcal{U}_{\beta_L, \beta_H}(\beta) \quad (\text{B8})$$

2. Draw  $n$  from the conditional marginalized distribution

$$P(n|\mu) := \int dp P(n, p|\mu), \quad (\text{B9})$$

3. Finally draw  $p$  from  $P(p|n, \mu)$ , i.e., from uniform distribution between  $p_{\min}(\mu)$  and  $p_{\max}(\mu, n)$ .

These steps are made simpler by the fact that the slice of  $V_{\beta_L, \beta_H}$  at fixed  $\mu$  is a triangle, making it trivial to find  $P(p|n, \mu)$  and  $P(n|\mu)$ . Lastly, the marginalized distribution  $P(\mu)$  can be straightforwardly computed and has the following form

$$P(\mu) = \begin{cases} \mu \frac{\mu^2 - \mu_L^2}{\mu_H^2 - \mu_L^2} C_1, & \mu_L < \mu < \mu_c, \\ \mu \frac{\mu_H^2 - \mu^2}{\mu_H^2 - \mu_c^2} C_2, & \mu_c < \mu < \mu_H, \end{cases} \quad (\text{B10})$$

where  $C_1$  and  $C_2$  are constants ensuring continuity at  $\mu_c$ . For convenience, we normalize the distribution such that  $P(\mu_c) = 1$ . Writing this distribution as a function of  $\mu^2$ , we have

$$P(\mu^2) d\mu^2 = d\mu^2 \begin{cases} \left[ \frac{\mu^2 - \mu_L^2}{\mu_c^2 - \mu_L^2} \right] \left[ \frac{\mu_H^2 - \mu^2}{\mu_H^2 - \mu_c^2} \right], & \mu_L^2 < \mu^2 < \mu_c^2, \\ \left[ \frac{\mu_H^2 - \mu^2}{\mu_H^2 - \mu_c^2} \right] \left[ \frac{\mu^2 - \mu_L^2}{\mu_c^2 - \mu_L^2} \right], & \mu_c^2 < \mu^2 < \mu_H^2. \end{cases} \quad (\text{B11})$$

To sample this distribution, we transform to a variable  $X(\mu^2) := \int d\mu^2 P(\mu^2)$ . The explicit form of  $X(\mu^2)$  can be found analytically

$$X(\mu^2) = \begin{cases} \frac{\mu_H^2 - \mu_c^2}{\mu_c^2 - \mu_L^2} \left[ -(\mu^2 - \mu_L^2) - (\mu_H^2 - \mu_L^2) \log \left( \frac{\mu_H^2 - \mu^2}{\mu_H^2 - \mu_L^2} \right) \right], & \mu_L^2 \leq \mu^2 \leq \mu_c^2, \\ \frac{\mu_c^2 - \mu_L^2}{\mu_H^2 - \mu_c^2} \left[ -(\mu^2 - \mu_c^2) + (\mu_H^2 - \mu_L^2) \log \left( \frac{\mu^2 - \mu_L^2}{\mu_c^2 - \mu_L^2} \right) \right], & \mu_c^2 \leq \mu^2 < \mu_H^2. \end{cases} \quad (\text{B12})$$

Finally, in order to sample  $P(\mu^2)$  we sample  $X$  from a uniform distribution and then transform back to  $\mu^2$  with the inverse function

$$\mu^2(X) = \begin{cases} \mu_H^2 + (\mu_c^2 - \mu_L^2) W \left( -\exp \left\{ -\frac{X \frac{\mu_H^2 - \mu_L^2}{\mu_H^2 - \mu_c^2} + (\mu_H^2 - \mu_L^2)}{\mu_H^2 - \mu_L^2} \right\} \right), & \mu_L^2 \leq \mu^2 \leq \mu_c^2, \\ \mu_L^2 - (\mu_c^2 - \mu_L^2) W \left( \frac{\mu_L^2 - \mu_c^2}{\mu_H^2 - \mu_c^2} \exp \left\{ \frac{X \frac{\mu_H^2 - \mu_c^2}{\mu_c^2 - \mu_L^2} + (\mu_L^2 - \mu_c^2)}{\mu_H^2 - \mu_L^2} \right\} \right), & \mu_c^2 < \mu^2 < \mu_H^2, \end{cases} \quad (\text{B13})$$

where  $W$  is the Lambert- $W$  function.

### C. CONDITION FOR THE CAUSALITY OF THE DIFFUSION

To ensure that the diffusion process preserves causality, the local sound speed must remain subluminal,  $0 < c_s^2 < 1$ , if it is initially within this range. We therefore recast the diffusion equation in terms of the sound speed  $c_s^2(n, \tau)$ ,

$$\begin{aligned} \partial_\tau c_s^2 &= D \partial_n^2 c_s^2 + \left( 2D' - (1 - c_s^2) \frac{2D}{n} \right) \partial_n c_s^2 \quad (\text{C14}) \\ &+ \left( \frac{2D}{n^2} - \frac{D'}{n} \right) (1 - c_s^2) c_s^2 + \left( D'' - \frac{D'}{n} \right) c_s^2 \end{aligned}$$

We next use a first-touch argument to determine conditions on  $D(n)$  that guarantee  $c_s^2$  remains within  $0 \leq c_s^2 \leq 1$  for all later times.

If  $c_s^2$  has an interior minimum with  $c_s^2 = 0$ , then  $\partial_n c_s^2 = 0$  and  $\partial_n^2 c_s^2 \geq 0$  there. Evaluating Eq. (C14) at that point gives

$$\partial_\tau c_s^2 = D \partial_n^2 c_s^2 > 0, \quad (\text{C15})$$

which is positive provided that  $D(n) > 0$  everywhere in the domain. The minimum value of  $c_s^2$  can only increase in  $\tau$  and therefore  $c_s^2$  cannot cross below zero.

Similarly, if  $c_s^2$  reaches an interior maximum with  $c_s^2 = 1$ , then  $\partial_n c_s^2 = 0$  and  $\partial_n^2 c_s^2 \leq 0$ . All terms proportional to  $(1 - c_s^2)$  vanish at that point, and Eq. (C14) reduces to

$$\partial_\tau c_s^2 = D \partial_n^2 c_s^2 + \left( D'' - \frac{D'}{n} \right) c_s^2 \quad (\text{C16})$$

This is guaranteed to be negative as long as the diffusion coefficient satisfies

$$D'' - \frac{D'}{n} \leq 0$$

for all  $n$  in the interval. Note, however, that the boundary conditions do not necessarily satisfy  $c_s^2 < 1$ . In this study, no EoS exhibits such behavior due to the extended diffusion range to chiral EFT and pQCD, where the values of the speed of sound are well below unity, as outlined in Section 3.

#### D. COVARIANCE OF THE SPEED OF SOUND AFTER DIFFUSION

In this appendix we demonstrate that the diffusion equation leads to Gaussian correlations for the speed of sound at short distances. The assumptions entering this derivation are as follows:

- Fluctuations of  $\mu(n)$  in the ensemble are small compared to its mean, so that the logarithm in the definition of the speed of sound can be expanded;
- The ensemble-averaged chemical potential  $\bar{\mu}(n)$  is a slowly varying function of density;
- The diffusion coefficient  $D(n)$  can be approximated locally as a constant; and
- The short-distance correlations of  $c_s^2$  can be approximated as nearly white, even though global structure of the EoS may induce long-range correlations. On the contrary, we do not assume anything about the correlations of  $\mu$ , which are non-trivial due to the constraint structure.

We compute the covariance of the sound speed at two densities  $n$  and  $n'$  after a diffusion time  $\tau$ :

$$\langle \delta c_s^2(n, \tau) \delta c_s^2(n', \tau) \rangle.$$

Assuming small fluctuations around the ensemble mean  $\bar{\mu}(n, \tau) := \langle \mu(n, \tau) \rangle$ , we write

$$\mu(n, \tau) = \bar{\mu}(n, \tau) + \delta\mu(n, \tau). \quad (\text{D17})$$

The speed of sound can then be expanded as

$$\begin{aligned} c_s^2(n, \tau) &= n \frac{\partial \log(\mu(n, \tau))}{\partial n} \\ &\approx n \partial_n \log \bar{\mu}(n, \tau) + n \partial_n \left( \frac{\delta\mu(n, \tau)}{\bar{\mu}(n, \tau)} \right). \end{aligned} \quad (\text{D18})$$

Because the ensemble mean varies slowly compared to individual realizations, its derivative in the second term induces corrections that are higher order and can be neglected. Hence, to the order we are working we can pull it through the derivative to obtain

$$\begin{aligned} c_s^2(n, \tau) &\approx n \partial_n \log \bar{\mu}(n, \tau) + \frac{n}{\bar{\mu}(n, \tau)} \partial_n \delta\mu(n, \tau) \\ &\approx \langle c_s^2(n, \tau) \rangle + \alpha \partial_n \delta\mu(n, \tau), \end{aligned} \quad (\text{D19})$$

where  $\alpha := n_0/\bar{\mu}(n_0, \tau)$  is treated as locally constant. In this equation, we used that the ensemble mean of the sound speed  $c_s^2(n, \tau)$  can be approximated by the derivative of the ensemble mean of  $\mu$

$$\langle c_s^2(n, \tau) \rangle = n \partial_n \log \bar{\mu}(n, \tau) + \mathcal{O}(\delta\mu^2, \delta\mu \partial_n \bar{\mu}). \quad (\text{D20})$$

The correlation function then reads

$$\langle \delta c_s^2(n, \tau) \delta c_s^2(n', \tau) \rangle \approx \alpha^2 \partial_n \partial_{n'} \langle \delta\mu(n, \tau) \delta\mu(n', \tau) \rangle. \quad (\text{D21})$$

Writing the evolved correlation function in terms of the initial condition and the Green function of the diffusion equation,

$$\begin{aligned} \langle \delta\mu(n, \tau) \delta\mu(n', \tau) \rangle & \\ &= \int d\xi d\xi' G(n, \xi; \tau) G(n', \xi'; \tau) \langle \delta\mu(\xi, 0) \delta\mu(\xi', 0) \rangle, \end{aligned} \quad (\text{D22})$$

we obtain

$$\begin{aligned} \langle \delta c_s^2(n, \tau) \delta c_s^2(n', \tau) \rangle & \\ &= \alpha^2 \int d\xi d\xi' \partial_n G(n, \xi; \tau) \partial_{n'} G(n', \xi'; \tau) \langle \delta\mu(\xi, 0) \delta\mu(\xi', 0) \rangle. \end{aligned} \quad (\text{D23})$$

Using the self-adjoint property of the diffusion operator, we can shift the derivatives from  $(n, n')$  to  $(\xi, \xi')$  and partially integrate the derivatives to act on the initial correlation

$$\begin{aligned} \langle \delta c_s^2(n, \tau) \delta c_s^2(n', \tau) \rangle & \\ &= \alpha^2 \int d\xi d\xi' G(n, \xi; \tau) G(n', \xi'; \tau) \langle \partial_\xi \delta\mu(\xi, 0) \partial_{\xi'} \delta\mu(\xi', 0) \rangle. \end{aligned} \quad (\text{D24})$$

Recognizing that  $\partial_\xi \delta\mu(\xi, 0)$  corresponds to fluctuations of the initial sound speed,

$$\langle \delta c_s^2(\xi, 0) \delta c_s^2(\xi', 0) \rangle = \frac{1}{\alpha^2} \langle \partial_\xi \delta\mu(\xi, 0) \partial_{\xi'} \delta\mu(\xi', 0) \rangle, \quad (\text{D26})$$

we can express the covariance as

$$\begin{aligned} \langle \delta c_s^2(n, \tau) \delta c_s^2(n', \tau) \rangle & \\ &= \int d\xi d\xi' G(n, \xi; \tau) G(n', \xi'; \tau) \langle \delta c_s^2(\xi, 0) \delta c_s^2(\xi', 0) \rangle. \end{aligned} \quad (\text{D27})$$

Assuming a nearly white initial correlation function for the sound speed,

$$\langle \delta c_s^2(\xi, 0) \delta c_s^2(\xi', 0) \rangle \approx \sigma_s^2 \delta(\xi - \xi'),$$

and using the Gaussian Green function of the diffusion equation

$$G(n, \xi; \tau) = \frac{1}{\sqrt{4\pi D\tau}} \exp\left[-\frac{(n - \xi)^2}{4D\tau}\right], \quad (\text{D28})$$

the integral yields

$$\langle \delta c_s^2(n, \tau) \delta c_s^2(n', \tau) \rangle \simeq \frac{\sigma_s^2}{\sqrt{8\pi D\tau}} \exp\left[-\frac{(n-n')^2}{8D\tau}\right]. \quad (\text{D29})$$

Thus, the diffusion equation transforms initially (nearly) white  $c_s^2$  fluctuations into Gaussian correlations with a

characteristic correlation length

$$\sigma = \sqrt{4D\tau} \quad (\text{D30})$$

At large separations the above approximations break down, and the global structure of the EoS may introduce long-range, non-Gaussian correlations. Nevertheless, at short distances the Gaussian form provides an excellent local approximation. The argument extends to spatially varying  $D(n)$  as long as  $D(n)$  varies slowly over the correlation length.

## REFERENCES

- Abbott, B. P., Abbott, R., Abbott, T. D., et al. 2017, GW170817: Observation of Gravitational Waves from a Binary Neutron Star Inspiral, *Phys. Rev. Lett.*, 119, 161101, doi: [10.1103/PhysRevLett.119.161101](https://doi.org/10.1103/PhysRevLett.119.161101)
- Abbott, B. P., Abbott, R., Abbott, T. D., et al. 2019, Properties of the Binary Neutron Star Merger GW170817, *Phys. Rev. X*, 9, 011001, doi: [10.1103/PhysRevX.9.011001](https://doi.org/10.1103/PhysRevX.9.011001)
- Al-Mamun, M., Steiner, A. W., Nättilä, J., et al. 2021, Combining Electromagnetic and Gravitational-Wave Constraints on Neutron-Star Masses and Radii, *Phys. Rev. Lett.*, 126, 061101, doi: [10.1103/PhysRevLett.126.061101](https://doi.org/10.1103/PhysRevLett.126.061101)
- Altiparmak, S., Ecker, C., & Rezzolla, L. 2022, On the Sound Speed in Neutron Stars, *Astrophys. J. Lett.*, 939, L34, doi: [10.3847/2041-8213/ac9b2a](https://doi.org/10.3847/2041-8213/ac9b2a)
- Annala, E., Gorda, T., Hirvonen, J., et al. 2023, Strongly interacting matter exhibits deconfined behavior in massive neutron stars, *Nature Commun.*, 14, 8451, doi: [10.1038/s41467-023-44051-y](https://doi.org/10.1038/s41467-023-44051-y)
- Annala, E., Gorda, T., Kurkela, A., Nättilä, J., & Vuorinen, A. 2020, Evidence for quark-matter cores in massive neutron stars, *Nature Phys.*, 16, 907, doi: [10.1038/s41567-020-0914-9](https://doi.org/10.1038/s41567-020-0914-9)
- Annala, E., Gorda, T., Kurkela, A., & Vuorinen, A. 2018, Gravitational-Wave Constraints on the Neutron-Star-Matter Equation of State, *Phys. Rev. Lett.*, 120, 172703, doi: [10.1103/PhysRevLett.120.172703](https://doi.org/10.1103/PhysRevLett.120.172703)
- Antoniadis, J., Freire, P. C. C., Wex, N., et al. 2013, A Massive Pulsar in a Compact Relativistic Binary, *Science*, 340, 1233232, doi: [10.1126/science.1233232](https://doi.org/10.1126/science.1233232)
- Arzoumanian, Z., Brazier, A., Burke-Spolaor, S., et al. 2018, The NANOGrav 11-year Data Set: High-precision timing of 45 Millisecond Pulsars, *Astrophys. J. Suppl.*, 235, 37, doi: [10.3847/1538-4365/aab5b0](https://doi.org/10.3847/1538-4365/aab5b0)
- Baiotti, L., & Rezzolla, L. 2017, Binary neutron star mergers: a review of Einstein’s richest laboratory, *Rept. Prog. Phys.*, 80, 096901, doi: [10.1088/1361-6633/aa67bb](https://doi.org/10.1088/1361-6633/aa67bb)
- Baym, G., Hatsuda, T., Kojo, T., et al. 2018, From hadrons to quarks in neutron stars: a review, *Rept. Prog. Phys.*, 81, 056902, doi: [10.1088/1361-6633/aaae14](https://doi.org/10.1088/1361-6633/aaae14)
- Baym, G., Pethick, C., & Sutherland, P. 1971, The Ground state of matter at high densities: Equation of state and stellar models, *Astrophys. J.*, 170, 299, doi: [10.1086/151216](https://doi.org/10.1086/151216)
- Capano, C. D., Tews, I., Brown, S. M., et al. 2020, Stringent constraints on neutron-star radii from multimessenger observations and nuclear theory, *Nature Astronomy*, 4, 625, doi: [10.1038/s41550-020-1014-6](https://doi.org/10.1038/s41550-020-1014-6)
- Cartaxo, J., Huang, C., Malik, T., et al. 2025, Covariant Energy Density Functionals for Neutron Star Matter Equation of State Modeling: Cross-Comparison Analysis Using `\textttCompactObject`, <https://arxiv.org/abs/2506.03112>
- Choudhury, D., Salmi, T., Vinciguerra, S., et al. 2024, A NICER View of the Nearest and Brightest Millisecond Pulsar: PSR J0437–4715, *Astrophys. J. Lett.*, 971, L20, doi: [10.3847/2041-8213/ad5a6f](https://doi.org/10.3847/2041-8213/ad5a6f)
- Demorest, P., Pennucci, T., Ransom, S., Roberts, M., & Hessels, J. 2010, Shapiro Delay Measurement of A Two Solar Mass Neutron Star, *Nature*, 467, 1081, doi: [10.1038/nature09466](https://doi.org/10.1038/nature09466)
- Dietrich, T., Coughlin, M. W., Pang, P. T. H., et al. 2020, Multimessenger constraints on the neutron-star equation of state and the Hubble constant, *Science*, 370, 1450, doi: [10.1126/science.abb4317](https://doi.org/10.1126/science.abb4317)
- Dittmann, A. J., et al. 2024, A More Precise Measurement of the Radius of PSR J0740+6620 Using Updated NICER Data, *Astrophys. J.*, 974, 295, doi: [10.3847/1538-4357/ad5f1e](https://doi.org/10.3847/1538-4357/ad5f1e)

- Drischler, C., Han, S., Lattimer, J. M., et al. 2021, Limiting masses and radii of neutron stars and their implications, *Phys. Rev. C*, 103, 045808, doi: [10.1103/PhysRevC.103.045808](https://doi.org/10.1103/PhysRevC.103.045808)
- Ecker, C., Gorda, T., Kurkela, A., & Rezzolla, L. 2025, Constraining the equation of state in neutron-star cores via the long-ringdown signal, *Nature Commun.*, 16, 1320, doi: [10.1038/s41467-025-56500-x](https://doi.org/10.1038/s41467-025-56500-x)
- Essick, R., Legred, I., Chatziioannou, K., Han, S., & Landry, P. 2023, Phase transition phenomenology with nonparametric representations of the neutron star equation of state, *Phys. Rev. D*, 108, 043013, doi: [10.1103/PhysRevD.108.043013](https://doi.org/10.1103/PhysRevD.108.043013)
- Essick, R., Tews, I., Landry, P., Reddy, S., & Holz, D. E. 2020, Direct Astrophysical Tests of Chiral Effective Field Theory at Supranuclear Densities, *Phys. Rev. C*, 102, 055803, doi: [10.1103/PhysRevC.102.055803](https://doi.org/10.1103/PhysRevC.102.055803)
- Finch, E., Legred, I., Chatziioannou, K., et al. 2025, Unified nonparametric equation-of-state inference from the neutron-star crust to perturbative-QCD densities, <https://arxiv.org/abs/2505.13691>
- Fonseca, E., Pennucci, T., Ellis, J., et al. 2016, The NANOGrav Nine-year Data Set: Mass and Geometric Measurements of Binary Millisecond Pulsars, *Astrophys. J.*, 832, 167, doi: [10.3847/0004-637X/832/2/167](https://doi.org/10.3847/0004-637X/832/2/167)
- Fonseca, E., Cromartie, H. T., Pennucci, T. T., et al. 2021, Refined Mass and Geometric Measurements of the High-mass PSR J0740+6620, *Astrophys. J. Lett.*, 915, L12, doi: [10.3847/2041-8213/ac03b8](https://doi.org/10.3847/2041-8213/ac03b8)
- Fujimoto, Y., Fukushima, K., Kamata, S., & Murase, K. 2024, Uncertainty quantification in the machine-learning inference from neutron star probability distribution to the equation of state, *Phys. Rev. D*, 110, 034035, doi: [10.1103/PhysRevD.110.034035](https://doi.org/10.1103/PhysRevD.110.034035)
- Fujimoto, Y., Fukushima, K., McLerran, L. D., & Praszalowicz, M. 2022, Trace Anomaly as Signature of Conformality in Neutron Stars, *Phys. Rev. Lett.*, 129, 252702, doi: [10.1103/PhysRevLett.129.252702](https://doi.org/10.1103/PhysRevLett.129.252702)
- Gasbarra, D., Sottinen, T., & Valkeila, E. 2007, Gaussian Bridges, in *Stochastic Analysis and Applications*, ed. F. E. Benth, G. Di Nunno, T. Lindström, B. Øksendal, & T. Zhang (Berlin, Heidelberg: Springer Berlin Heidelberg), 361–382, doi: [10.1007/978-3-540-70847-6\\_15](https://doi.org/10.1007/978-3-540-70847-6_15)
- Gorda, T., Hebeler, K., Kurkela, A., Schwenk, A., & Vuorinen, A. 2023a, Constraints on Strong Phase Transitions in Neutron Stars, *Astrophys. J.*, 955, 100, doi: [10.3847/1538-4357/aceefb](https://doi.org/10.3847/1538-4357/aceefb)
- Gorda, T., Komoltsev, O., & Kurkela, A. 2023b, Ab-initio QCD Calculations Impact the Inference of the Neutron-star-matter Equation of State, *Astrophys. J.*, 950, 107, doi: [10.3847/1538-4357/acce3a](https://doi.org/10.3847/1538-4357/acce3a)
- Gorda, T., Komoltsev, O., Kurkela, A., & Mazeliauskas, A. 2023c, Bayesian uncertainty quantification of perturbative QCD input to the neutron-star equation of state, *JHEP*, 06, 002, doi: [10.1007/JHEP06\(2023\)002](https://doi.org/10.1007/JHEP06(2023)002)
- Gorda, T., Kurkela, A., Paatelainen, R., Säppi, S., & Vuorinen, A. 2021, Soft Interactions in Cold Quark Matter, *Phys. Rev. Lett.*, 127, 162003, doi: [10.1103/PhysRevLett.127.162003](https://doi.org/10.1103/PhysRevLett.127.162003)
- Gorda, T., Paatelainen, R., Säppi, S., & Seppänen, K. 2023d, Equation of State of Cold Quark Matter to  $O(\alpha_s^3 \ln \alpha_s)$ , *Phys. Rev. Lett.*, 131, 181902, doi: [10.1103/PhysRevLett.131.181902](https://doi.org/10.1103/PhysRevLett.131.181902)
- Hebeler, K., Lattimer, J. M., Pethick, C. J., & Schwenk, A. 2013, Equation of state and neutron star properties constrained by nuclear physics and observation, *Astrophys. J.*, 773, 11, doi: [10.1088/0004-637X/773/1/11](https://doi.org/10.1088/0004-637X/773/1/11)
- Hinderer, T., Lackey, B. D., Lang, R. N., & Read, J. S. 2010, Tidal deformability of neutron stars with realistic equations of state and their gravitational wave signatures in binary inspiral, *Phys. Rev. D*, 81, 123016, doi: [10.1103/PhysRevD.81.123016](https://doi.org/10.1103/PhysRevD.81.123016)
- Huth, S., Pang, P. T. H., Tews, I., et al. 2022, Constraining neutron-star matter with microscopic and macroscopic collisions, *Nature*, 606, 276, doi: [10.1038/s41586-022-04750-w](https://doi.org/10.1038/s41586-022-04750-w)
- Kärkkäinen, A., Navarrete, P., Nurmela, M., et al. 2025, Quark Matter at Four Loops: Hardships and How to Overcome Them, *Phys. Rev. Lett.*, 135, 021901, doi: [10.1103/627n-5g6l](https://doi.org/10.1103/627n-5g6l)
- Koehn, H., et al. 2025, From existing and new nuclear and astrophysical constraints to stringent limits on the equation of state of neutron-rich dense matter, *Phys. Rev. X*, 15, 021014, doi: [10.1103/PhysRevX.15.021014](https://doi.org/10.1103/PhysRevX.15.021014)
- Komoltsev, O. 2024, First-order phase transitions in the cores of neutron stars, *Phys. Rev. D*, 110, L071502, doi: [10.1103/PhysRevD.110.L071502](https://doi.org/10.1103/PhysRevD.110.L071502)
- Komoltsev, O. 2025, Perturbative QCD reveals the softening of matter in the cores of massive neutron stars, PhD thesis, Stavanger U. <https://arxiv.org/abs/2506.06465>
- Komoltsev, O., & Kurkela, A. 2022, How Perturbative QCD Constrains the Equation of State at Neutron-Star Densities, *Phys. Rev. Lett.*, 128, 202701, doi: [10.1103/PhysRevLett.128.202701](https://doi.org/10.1103/PhysRevLett.128.202701)

- Komoltsev, O., Somasundaram, R., Gorda, T., et al. 2024, Equation of state at neutron-star densities and beyond from perturbative QCD, *Phys. Rev. D*, 109, 094030, doi: [10.1103/PhysRevD.109.094030](https://doi.org/10.1103/PhysRevD.109.094030)
- Kurkela, A., Fraga, E. S., Schaffner-Bielich, J., & Vuorinen, A. 2014, Constraining neutron star matter with Quantum Chromodynamics, *Astrophys. J.*, 789, 127, doi: [10.1088/0004-637X/789/2/127](https://doi.org/10.1088/0004-637X/789/2/127)
- Landry, P., & Essick, R. 2019, Nonparametric inference of the neutron star equation of state from gravitational wave observations, *Phys. Rev. D*, 99, 084049, doi: [10.1103/PhysRevD.99.084049](https://doi.org/10.1103/PhysRevD.99.084049)
- Landry, P., Essick, R., & Chatziioannou, K. 2020, Nonparametric constraints on neutron star matter with existing and upcoming gravitational wave and pulsar observations, *Phys. Rev. D*, 101, 123007, doi: [10.1103/PhysRevD.101.123007](https://doi.org/10.1103/PhysRevD.101.123007)
- Legred, I., Chatziioannou, K., Essick, R., & Landry, P. 2022, Implicit correlations within phenomenological parametric models of the neutron star equation of state, *Phys. Rev. D*, 105, 043016, doi: [10.1103/PhysRevD.105.043016](https://doi.org/10.1103/PhysRevD.105.043016)
- Lim, Y., & Holt, J. W. 2022, Neutron Star Radii, Deformabilities, and Moments of Inertia from Experimental and Ab Initio Theory Constraints of the  $^{208}\text{Pb}$  Neutron Skin Thickness, *Galaxies*, 10, 99, doi: [10.3390/galaxies10050099](https://doi.org/10.3390/galaxies10050099)
- Mauviard, L., Guillot, S., Salmi, T., et al. 2025, A NICER view of the 1.4 solar-mass edge-on pulsar PSR J0614–3329, <https://arxiv.org/abs/2506.14883>
- Miller, M. C., Lamb, F. K., Dittmann, A. J., et al. 2019, PSR J0030+0451 Mass and Radius from NICER Data and Implications for the Properties of Neutron Star Matter, *Astrophys. J. Lett.*, 887, L24, doi: [10.3847/2041-8213/ab50c5](https://doi.org/10.3847/2041-8213/ab50c5)
- Miller, M. C., Lamb, F. K., Dittmann, A. J., et al. 2021, The Radius of PSR J0740+6620 from NICER and XMM-Newton Data, *Astrophys. J. Lett.*, 918, L28, doi: [10.3847/2041-8213/ac089b](https://doi.org/10.3847/2041-8213/ac089b)
- Mroczek, D., Miller, M. C., Noronha-Hostler, J., & Yunes, N. 2024, Nontrivial features in the speed of sound inside neutron stars, *Phys. Rev. D*, 110, 123009, doi: [10.1103/PhysRevD.110.123009](https://doi.org/10.1103/PhysRevD.110.123009)
- Oertel, M., Hempel, M., Klähn, T., & Typel, S. 2017, Equations of state for supernovae and compact stars, *Rev. Mod. Phys.*, 89, 015007, doi: [10.1103/RevModPhys.89.015007](https://doi.org/10.1103/RevModPhys.89.015007)
- Oppenheimer, J. R., & Volkoff, G. M. 1939, On massive neutron cores, *Phys. Rev.*, 55, 374, doi: [10.1103/PhysRev.55.374](https://doi.org/10.1103/PhysRev.55.374)
- Raaijmakers, G., Greif, S. K., Hebeler, K., et al. 2021, Constraints on the Dense Matter Equation of State and Neutron Star Properties from NICER’s Mass–Radius Estimate of PSR J0740+6620 and Multimessenger Observations, *The Astrophysical Journal Letters*, 918, L29, doi: [10.3847/2041-8213/ac089a](https://doi.org/10.3847/2041-8213/ac089a)
- Riley, T. E., Watts, A. L., Bogdanov, S., et al. 2019, A NICER View of PSR J0030+0451: Millisecond Pulsar Parameter Estimation, *The Astrophysical Journal Letters*, 887, L21, doi: [10.3847/2041-8213/ab481c](https://doi.org/10.3847/2041-8213/ab481c)
- Riley, T. E., Watts, A. L., Ray, P. S., et al. 2021, A NICER View of the Massive Pulsar PSR J0740+6620 Informed by Radio Timing and XMM-Newton Spectroscopy, *Astrophys. J. Lett.*, 918, L27, doi: [10.3847/2041-8213/ac0a81](https://doi.org/10.3847/2041-8213/ac0a81)
- Saffer, A., Fonseca, E., Ransom, S., et al. 2025, A Lower Mass Estimate for PSR J0348+0432 Based on CHIME/Pulsar Precision Timing, *Astrophys. J. Lett.*, 983, L20, doi: [10.3847/2041-8213/adc25e](https://doi.org/10.3847/2041-8213/adc25e)
- Semposki, A. C., Drischler, C., Furnstahl, R. J., & Phillips, D. R. 2025, Microscopic constraints for the equation of state and structure of neutron stars: a Bayesian model mixing framework, <https://arxiv.org/abs/2505.18921>
- Somasundaram, R., Tews, I., & Margueron, J. 2023, Perturbative QCD and the neutron star equation of state, *Phys. Rev. C*, 107, L052801, doi: [10.1103/PhysRevC.107.L052801](https://doi.org/10.1103/PhysRevC.107.L052801)
- Steiner, A. W., Lattimer, J. M., & Brown, E. F. 2016, Neutron Star Radii, Universal Relations, and the Role of Prior Distributions, *Eur. Phys. J. A*, 52, 18, doi: [10.1140/epja/i2016-16018-1](https://doi.org/10.1140/epja/i2016-16018-1)
- Tews, I., Margueron, J., & Reddy, S. 2018, Critical examination of constraints on the equation of state of dense matter obtained from GW170817, *Phys. Rev. C*, 98, 045804, doi: [10.1103/PhysRevC.98.045804](https://doi.org/10.1103/PhysRevC.98.045804)
- Tolman, R. C. 1939, Static solutions of Einstein’s field equations for spheres of fluid, *Phys. Rev.*, 55, 364, doi: [10.1103/PhysRev.55.364](https://doi.org/10.1103/PhysRev.55.364)